Constructing Time-Varying Directed EEG Network by Multivariate Nonparametric Dynamical Granger Causality

Chanlin Yi, Yuan Qiu, Wanjun Chen, Chunli Chen, Yifeng Wang, Peiyang Li, Lei Yang, Xiabing Zhang, Lin Jiang, Dezhong Yao, Fali Li, and Peng Xu

***Abstract*— Time-varying directed electroencephalography (EEG) network is the potential tool for studying the dynamical causality among brain areas at a millisecond level; which conduces to understanding how our brain effectively adapts to information processing, giving inspiration to causality- and brain-inspired machine learning. Currently, its construction still mainly relies on the parametric approach such as multivariate adaptive autoregressive (MVAAR), represented by the most widely used adaptive directed transfer function (ADTF). Restricted by the model assumption, the corresponding performance largely depends on the MVAAR modeling which usually encounters difficulty in fitting complex spectral features. In this study, we proposed to construct EEG directed network with multivariate nonparametric dynamical Granger causality (mndGC) method that infers the causality of a network, instead, in a data-driven way directly and therefore avoids the trap in the model-dependent parametric approach. Comparisons between mndGC and ADTF were conducted both with simulation and real data application. Simulation study demonstrated the superiority of mndGC both in noise resistance and capturing the instantaneous directed network changes. When applying to the real motor imagery (MI) data set, distinguishable network characters between left- and right-hand MI during different MI stages were better revealed by mndGC. Our study extends the nonparametric causality exploration and provides practical suggestions for the time-varying directed EEG network analysis.**

***Index Terms*— ADTF, brain networks, EEG, motor imagery, multivariate nonparametric dynamical Granger causality (mndGC).**

Manuscript received February 19, 2022; revised April 24, 2022; accepted May 10, 2022. Date of publication May 16, 2022; date of current version May 31, 2022. This work was supported in part by the National Natural Science Foundation of China under Grant 61961160705, Grant U19A2082, and Grant 62103085; in part by the Project of Science and Technology Department of Sichuan Province under Grant 2021YFSY0040 and Grant 2020ZYD013; and in part by the Science and Technology Development Fund, Macau Special Administrative Region (SAR) under Grant 0045/2019/AFJ. *(Chanlin Yi and Yuan Qiu contributed equally to this work.) (Corresponding authors: Peng Xu; Fali Li.)*

This work involved human subjects or animals in its research. Approval of all ethical and experimental procedures and protocols was granted by the Ethics Committee of the University of Electronic Science and Technology of China (UESTC).

Chanlin Yi, Yuan Qiu, Wanjun Chen, Chunli Chen, Yifeng Wang, Lei Yang, Xiabing Zhang, and Lin Jiang are with the Clinical Hospital of Chengdu Brain Science Institute, MOE Key Laboratory for Neuroinformation, and the School of Life Science and Technology, Center for Information in Medicine, University of Electronic Science and Technology of China, Chengdu 611731, China.

Peiyang Li is with the School of Bioinformatics, Chongqing University of Posts and Telecommunications, Chongqing 400065, China.

Dezhong Yao is with the Clinical Hospital of Chengdu Brain Science Institute, MOE Key Laboratory for Neuroinformation, and the School of Life Science and Technology, Center for Information in Medicine, University of Electronic Science and Technology of China, Chengdu 611731, China, also with the Research Unit of NeuroInformation, Chinese Academy of Medical Sciences, Chengdu 100006, China, and also with the School of Electrical Engineering, Zhengzhou University, Zhengzhou 450001, China.

Fali Li is the Clinical Hospital of Chengdu Brain Science Institute, MOE Key Laboratory for Neuroinformation, and the School of Life Science and Technology, Center for Information in Medicine, University of Electronic Science and Technology of China, Chengdu 611731, China, and also with the Research Unit of NeuroInformation, Chinese Academy of Medical Sciences, Chengdu 100006, China (e-mail: fali.li@uestc.edu.cn).

Peng Xu is with the Clinical Hospital of Chengdu Brain Science Institute, MOE Key Laboratory for Neuroinformation, and the School of Life Science and Technology, Center for Information in Medicine, University of Electronic Science and Technology of China, Chengdu 611731, China, and also with the Radiation Oncology Key Laboratory of Sichuan Province, Chengdu 610041, China (e-mail: xupeng@uestc.edu.cn).

This article has supplementary downloadable material available at https://doi.org/10.1109/TNSRE.2022.3175483, provided by the authors.

Digital Object Identifier 10.1109/TNSRE.2022.3175483

I. Introduction

OUR brain works as a complex network, in which the functional connectivity among vast brain areas changes quickly to guarantee the accomplishment of the brain activity strictly, orderly, and efficiently [1], [2]. A comprehensive understanding of the brain functions requires an exploration of the functional connectivity with directed information and dynamics [3]–[7] and knowledge of brain network has been widely applicated in cognition, disease, and engineering research [8]–[11]. Exploring the time-varying directed networks would not only help to understand how the brain areas affect each other and how it changes during a specific cognition process but also conduce to uncover the potential intervention strategies, including where, when, and how to intervene [12], [13]. Due to such merits as high time resolution, non-invasiveness, mobility, and easy operation of electroencephalography (EEG) [14]–[16], the time-varying directed EEG network is particularly suited for exploring the dynamical activities in our brain, as well as the instantaneous causality network patterns [17], [18]. For instance, by performing the time-varying EEG network analysis, Song *et al.* revealed that low-frequency repetitive transcranial magnetic

stimulation (rTMS) targeting the right posterior parietal cortex has significantly positive effects on the treatment of primary insomnia, the curative effect lasted at least one month [19].

Currently, in time-varying directed connectivity analysis, the mainstream methods are based on the parametric framework that requires a specification of a model [13], [20]. Based on the time-variant multivariate autoregressive (MVAR) model, multiple methods were proposed with different causality definitions for time-varying directed connectivity analysis, such as adaptive directed transfer function (ADTF), adaptive partial directed coherence, and adaptive Granger causality (GC) [20]. Due to the differences in time-variant MVAR model calculation and normalizations, several extensions also emerged [20], [21]. Although there are numerous parametric methods, in time-varying directed EEG network construction, the most widely used method is ADTF because of its good performance in interpretations and accurately capturing of the time-variant causality between signals [22], [23]. For instance, using EEG time-varying directed network analysis by ADTF, Si *et al.* revealed the diverse network patterns during the different decision stages and distinguishable patterns between different types of responses to the unfair offer [17]. However, restricted by the model assumptions, such parametric approaches rely a lot on accurate signal modeling. The autoregressive (AR) modeling process needs enough data to enable the attractor construction in phase space and the data size needs grows exponentially with the dimension of the attractor, therefore, it is often paralyzed in fitting the complex spectral characters that require higher-order AR models [24]. Whereas, EEG-like neurobiological signals are non-stationary with complex spectral representations [24]–[27]. Also, the model order determination remains a concern, although multiple methods based on the Bayesian framework were proposed to mitigate such effect [28]–[30].

The nonparametric Granger causality is first presented by Dhamala *et al.* in 2008 [31]. Specifically, it derives the noise covariance and transfer function out of the cross-spectral density of the two sequences through the non-parametric spectral matrix factorization and embeds them into Geweke's frequency-domain Granger causality (GC) method [32]. It jumps out of the conventional GC framework that is widely used in the field of neuroscience and infers the causality relationships directly from the data itself in a data-driven way, therefore, completely avoiding the delicate step of estimating parameters and modeling signals. Without the model restrictions, it is comparatively more flexible in practical applications. In recent years, this method was also extended into the multivariate and time-variant context by introducing the wavelet transform for time-varying cross-spectral density calculation and the multivariate GC estimation, which result in the multivariate nonparametric dynamical Granger causality (mndGC) [33]–[35]. Multiple studies have demonstrated that the nonparametric scheme is more flexible in statistical tests, can achieve very comparable performance to parametric approaches, and has considerable application values in causality analysis between two systems [34]–[36]. The nonparametric approaches have been applied in multiple neuroscience studies and reported many novel discoveries. For instance, Honjoh *et al.* revealed the causality modulation of the ventromedial thalamic nucleus (VM) on cortical activities and arouse, i.e., uncoupled and desynchronized cortical local circuits [37]. Considering the EEG data contains plenty of frequency oscillations and spectrum responses that play a crucial role in understanding the brain cognition processes [25], [38], [39], the spectral-based mndGC is particularly applicable for discovering such rhythm-based causality relationships.

Motor imagery (MI) is defined as a perception-like process with a variety of mental body movements without actual physical output and has wide applications in brain-computer interface (BCI), movement enhancement, and motor function rehabilitation [40], [41]. MI involves complex cognition processing like sensory information reception and integration, memory processing, and motor planning [40], [42], as well as shows distinct hemisphere synchronization and desynchronization characters between left- and right-hand MI during different stages [43]. Investigating its time-varying directed network is of great importance for understanding the corresponding dynamical working mechanisms and finding out the relevant intervention targets.

In this study, considering the parametric trap that time-varying directed EEG network construction often faces, we introduce the mndGC instead of the most widely used parametric method ADTF. Comparisons were performed between the mndGC and ADTF straightforwardly both in simulation data and real MI EEG data set to find practical experiences for the exploration of nonparametric time-varying directed EEG network construction.

The remainder of this article is organized as follows. Section II provides the methodological motivations and derivations of mndGC and ADTF. Section III shows the simulation and real MI EEG data set application details and results. Then, Section IV discuss the findings of this study, and finally, the conclusion of this study is described in Section V.

II. Methodology

The methodology of mndGC and ADTF is presented in this section.

A. Parametric Time-Varying Directed EEG Network: ADTF

Given L EEG time series $X = [x_1(t), x_2(t), \ldots, x_L(t)]$, $t = 1, \ldots, T$, ADTF [22] describes their time-varying linear coupling among the L multi-channel EEG signals with the following MVAAR model,

$$X(t) = \sum_{p=1}^{P} A_p(t) X(t-p) + E(t) \tag{1}$$

where P is the model order that is often determined by experience or information criterion methods like the Akaike Information Criterion (AIC) and the Schwarz Bayesian Criterion (SBC) [29], [30]; and $A_p(t) \in \mathbb{R}^{(L\times L)}$ is the MVAAR coefficient matrix at pth-order, in which each element indicates the dynamic causal influence of x_n on x_m at time point t; $E(t)$ is model noise that measures the prediction performance. In the implementation, by treating $A_p(t) \in \mathbb{R}^{(L\times L)}$ at each

time point t as a state, the Kalman filter is adopted to estimate it [22]. After Kalman estimation, in ADTF, the directed information matrix between any pairs of time series at time t and frequency f is defined as,

$$H_{mn}(t,f) = A^{-1}(t,f) = \left[\sum_{p=0}^{P} A_p(t)e^{-j2\pi f \Delta tp}\right]^{-1} \quad m = 1,\ldots,L, n = 1,\ldots,L \tag{2}$$

where superscripts "-1" denotes the inverse of a matrix. Each element in $H_{mn}(t,f)$ represents the information flow from signal x_n to x_m. In practice, we always adopt the normalized ADTF value that ranges from 0 to 1 as,

$$\gamma_{n\to m}(t,f) = |H_{mn}(t,f)| \Big/ \sum_{n=1}^{L} \left|H_{mn}^2(t,f)\right| \tag{3}$$

Finally, the time-varying effective connectivity matrix with each element representing the information flow between pairwise signals is,

$$ADTF(:,:,t) = \begin{bmatrix} \gamma_{1\to1}(t) & \gamma_{1\to2}(t) & \cdots & \gamma_{1\to L}(t) \\ \gamma_{2\to1}(t) & \gamma_{2\to2}(t) & \cdots & \gamma_{2\to L}(t) \\ \vdots & \vdots & \ddots & \vdots \\ \gamma_{L\to1}(t) & \gamma_{L\to2}(t) & \cdots & \gamma_{L\to L}(t) \end{bmatrix} \tag{4}$$

where $\gamma_{n\to m}(t)$ is the mean value of $\gamma_{n\to m}(t,f)|_{f\in\Theta}$ over a selected frequency band set Θ. Then, the ADTF values between pairwise signals make up the time-varying directed EEG network.

As shown in the above procedures, the causality estimation relies on the MVAAR modeling process. Such a parametric approach is model-dependent, which might cause illness in accurately determining the model parameter and fail to capture the complex spectral characters [24], [35].

B. Nonparametric Time-Varying Directed EEG Network: mndGC

For time series x_m and x_n in X as aforementioned, the mathematical derivation of the mndGC is given below. Wavelet transform is competitive for time-frequency analysis and presents the local time-frequency representations adaptively [44]. Therefore, to reveal the time-variant driving relationships among multivariate signals, mndGC defines the $S(f)$ in the space of the wavelet spectrum.

Theoretically, the continuous wavelet transform (CWT) of signals x_m and x_n in X at time point t and scale s is,

$$\begin{aligned} W_m(t,s) &= (1/\sqrt{s}) \int_{-\infty}^{+\infty} x_m(\eta)\psi^*((\eta - t)/s)d\eta \\ W_n(t,s) &= (1/\sqrt{s}) \int_{-\infty}^{+\infty} x_n(\eta)\psi^*((\eta - t)/s)d\eta \end{aligned} \tag{5}$$

where superscript "$*$" denotes the complex conjugate, $\psi(\eta)$ is the chosen mother wavelet, here, is Morlet wavelet formulated as,

$$\psi(\eta) = \pi^{-1/4} e^{j\omega\eta} e^{-\eta^2/2} \tag{6}$$

In fact, there is a one-to-one equivalence between scale s and frequency f. Thus, the $W_m(t,s)$ and $W_n(t,s)$ can be transformed to $W_m(t,f)$ and $W_n(t,f)$ directly. Consequently, the cross wavelet transform between any pairs of signals x_m and x_n in X holds the form as,

$$W_{mn}(t,f) = < W_m(t,f) W_n^*(t,f) > \tag{7}$$

with $<\cdot>$ being the expectation taking over all the trials [35]. The wavelet spectral matrix consists of cross-spectrum and self-spectrum between x_m and x_n at time point t has form as,

$$S(t,f) = \begin{bmatrix} W_{mm}(t,f) & W_{mn}(t,f) \\ W_{nm}(t,f) & W_{nn}(t,f) \end{bmatrix} \tag{8}$$

where $W_{mn}(t,f)$ and $W_{nm}(t,f)$ are the cross-spectrum between x_m and x_n, $W_{mm}(t,f)$ and $W_{nn}(t,f)$ are the self-spectrum of x_m and x_n. Then, $S(t,f)$ can be used to estimate the time-variant noise covariance matrix $\Sigma(t)$ and transfer function matrix $H(t,f)$, which is realized in this study by the high-efficiency Wilson spectral matrix factorization method [45], [46]. Specifically, the symmetric $S(t,f)$ can be represented as,

$$S(t,f) = \Psi\Psi^H \tag{9}$$

where Ψ denotes minimum-phase spectral function and superscript "H" denotes the complex conjugate transpose. In frequency theory, Ψ has Fourier expansion and its Fourier coefficients can be computed as,

$$C^k = \frac{1}{2\pi}\int_{-\pi}^{\pi} \Psi\left(e^{i\theta}\right) e^{-ik\theta} d\theta \tag{10}$$

where $\Psi\left(e^{i\theta}\right) e^{-ik\theta}$ is the Fourier operator. Therefore, the noise covariance matrix Σ and transfer function matrix H between x_{l_i} and x_{l_j} can be computed as,

$$\begin{aligned} \sum &= C^0 (C^0)^T \\ H &= \Psi (C^0)^{-1} \end{aligned} \tag{11}$$

Here, superscript "T" denotes matrix transpose. Combining (9), (10), and (11), the wavelet spectral matrix $S(t,f)$ can be further represented as $H\Sigma H^H$. Therefore, based on the definition of frequency GC [32], the nonparametric GC value at time t and frequency f can be computed as,

$$F_{n\to m}(t,f) = \ln\left(\frac{S_{mm}(t,f)}{S_{mm}(t,f) - \left(\sum_{nn}\left(-\left(\sum_{mn}\right)^2 \Big/ \sum_{mm}\right)|H_{mn}|^2\right)}\right) \tag{12}$$

where the numeric subscripts indicate the corresponding elements in the matrix $S(t,f)$, $\sum(t)$, and $H(t,f)$. Finally, the GC connectivity matrix at each time and frequency point can be obtained by calculating the GC strength $F_{l_j\to l_i}(t,f)$ between the pairwise signals as,

$$mndGC(:,:,t) = \begin{bmatrix} F_{1\to1}(t) & F_{1\to2}(t) & \cdots & F_{1\to L}(t) \\ F_{2\to1}(t) & F_{2\to2}(t) & \cdots & F_{2\to L}(t) \\ \vdots & \vdots & \ddots & \vdots \\ F_{L\to1}(t) & F_{L\to2}(t) & \cdots & F_{L\to L}(t) \end{bmatrix} \tag{13}$$

Algorithm 1: Time-Varying Directed EEG Network Construction

Input: multivariate signals set $X = [x_1, x_2, \cdots, x_L] \in \mathbb{R}^{L\times T}$ and the selected frequency band index set Θ.
Output: mndGC matrix $mndGC \in \mathbb{R}^{L\times L\times T}$.
01: Initializing: $m = 1, n = 1, t = 1$
02: For $m = 1 \rightarrow L$ do
03: For $n = 1 \rightarrow L$ do
04: $W_m(t,f) \leftarrow CWT(x_m), W_n(t,f) \leftarrow CWT(x_n)$;
05: $W_{mm}(t,f) \leftarrow < W_m(t,f)W_m^*(t,f) >, W_{mn}(t,f) \leftarrow < W_m(t,f)W_n^*(t,f) >,$ $W_{nm}(t,f) \leftarrow < W_n(t,f)W_m^*(t,f) >, W_{nn}(t,f) \leftarrow < W_n(t,f)W_n^*(t,f) >$;
06: $S(t,f) \leftarrow \begin{bmatrix} W_{mm}(t,f) & W_{mn}(t,f) \\ W_{nm}(t,f) & W_{nn}(t,f) \end{bmatrix}$;
07: For $t = 1 \rightarrow T$
08: $\Psi \leftarrow WMF(S(t,f))$;
09: $C^0 \leftarrow (1/2\pi)\int_{-\pi}^{\pi} \Psi(e^{i\theta})d\theta$;
10: $\Sigma \leftarrow C^0(C^0)^T, H \leftarrow \Psi(C^0)^{-1}$;
11: $F_{n\rightarrow m}(t,f) \leftarrow \ln(\frac{S_{mm}(t,f)}{S_{mm}(t,f)-(\sum_{mn}-(\sum_{mn})^2/\sum_{mm})|H_{mn}|^2})$
12: $F_{n\rightarrow m}(m,n,t) \leftarrow mean(F_{n\rightarrow m}(t,f)\big|_{f\in\Theta})$;
13: END for
14: END for
15: END for
16: END the procedure

The $CWT(\cdot)$ means the continuous wavelet transform, $WMF(\cdot)$ represents matrix factorization through Wilson's algorithm, $mean(\cdot)$ denotes mean value across the concerned frequency bands, and <·> denotes averaging all trials.

where the $F_{n\rightarrow m}(t)$ is the average granger causality strength across a given frequency set Θ at the time point t between signals x_m and x_n. The procedures of the proposed nonparametric time-varying directed network construction approach can be summarized in Algorithm 1.

By using spectral matrix factorization to estimate noise variances and inferring the Granger causal relationship through the cross-spectrum between paired time series, the proposed method avoids the model dependency and parameter trap usually encountered in the traditional parametric GC model.

III. Results

To evaluate the efficiency of mndGC and ADTF in time-varying directed network EEG construction, both simulation study and real MI EEG application were conducted. In the following experiments, consistent with previous studies [17], [29], Akaike Information Criterion (AIC) was used to estimate the model order on each trial for ADTF.

A. Simulation Experiments

1) Simulation Procedures: Firstly, a 5-node time-varying directed network (Fig.1) which characterized the causal relationship between 5 jointly stationary stochastic processes was predefined based on a three-order MVAAR model as,

$$\begin{aligned}
x_1(t) &= \varepsilon_1(t) - 0.35x_1(t-1) + 0.2x_1(t-2) \\
x_2(t) &= \varepsilon_2(t) - 0.25x_2(t-1) + a_{12}(t)x_1(t-2) \\
&\quad + a_{52}(t)x_5(t-3) \\
x_3(t) &= \varepsilon_3(t) - 0.25x_3(t-1) + a_{23}(t)x_2(t-2) \\
&\quad + a_{13}(t)x_1(t-3) \\
x_4(t) &= \varepsilon_4(t) - 0.25x_4(t-1) + a_{24}(t)x_2(t-2) \\
&\quad + a_{34}(t)x_3(t-2) + a_{14}(t)x_1(t-3) \\
x_5(t) &= \varepsilon_5(t) - 0.35x_5(t-1) + 0.2x_5(t-2) \\
&\quad + a_{25}(t)x_2(t-2) + a_{45}(t)x_4(t-2)
\end{aligned} \tag{14}$$

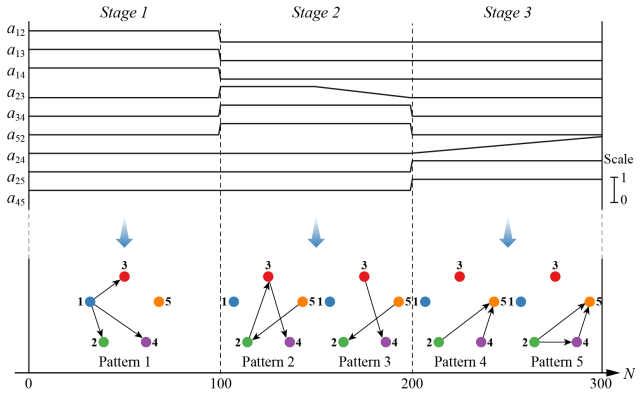

Fig. 1. The predefined time-varying directed network: the black lines on the top are the MVAAR coefficients that indicate the dynamical causality among the 5 nodes; below it, the subfigures denote the corresponding time-varying directed network patterns in the three stages defined by the MVAAR model, in which each solid circle represents a subnetwork, and the black arrow denotes the information flow in the network.

where $\varepsilon_l(t), l = 1, 2, \ldots, 5$ denotes the white noise with mean 0 and variance 0.25, $a_{mn}(t)$ is the MVAAR coefficient represents the dynamical influence between x_m and x_n at discrete-time index t. The predefined functions for the MVAAR coefficients are given below,

Coefficients $a_{12}(t)$ $a_{13}(t)$, and $a_{14}(t)$ were step functions as,

$$a_{l_i l_j}(t) = \begin{cases} 0.6 & 0 < t \le 100 \\ 0 & otherwise \end{cases} \tag{15}$$

Coefficients $a_{23}(t)$ and $a_{24}(t)$ were piecewise functions formulated as,

$$\begin{aligned}
a_{23}(t) &= \begin{cases} 0.6 & 100 < t \le 150 \\ -\dfrac{0.6}{50}(t-200) & 150 < t \le 200 \\ 0 & otherwise \end{cases} \\
a_{24}(t) &= \begin{cases} 0.9(\dfrac{t-200}{100}) & 200 < t \le 300 \\ 0 & otherwise \end{cases}
\end{aligned} \tag{16}$$

Coefficients $a_{34}(t)$ and $a_{52}(t)$ had the same function type, as well as $a_{25}(t)$ and $a_{45}(t)$. Their formulations were,

$$\begin{aligned}
a_{34}(t) = a_{52}(t) &= \begin{cases} 0.6 & 100 < t \le 200 \\ 0 & otherwise \end{cases} \\
a_{25}(t) = a_{45}(t) &= \begin{cases} 0.6 & 200 < t \le 300 \\ 0 & otherwise \end{cases}
\end{aligned} \tag{17}$$

As shown in Fig. 1, in a specific stage, the $a_{23}(t)$ and $a_{24}(t)$ would gradually change, while the other coefficients have fixed values. Correspondingly, the network changes over time, in which stage 1 has a fixed pattern (i.e., pattern 1), while stages 2 and 3 have changing patterns (i.e., as time goes by, the network would change from pattern 2 to pattern 3 due to the linear decrease of a_{23} in stage 2, and from pattern 4 to pattern 5 due to increase of a_{24} in stage 3).

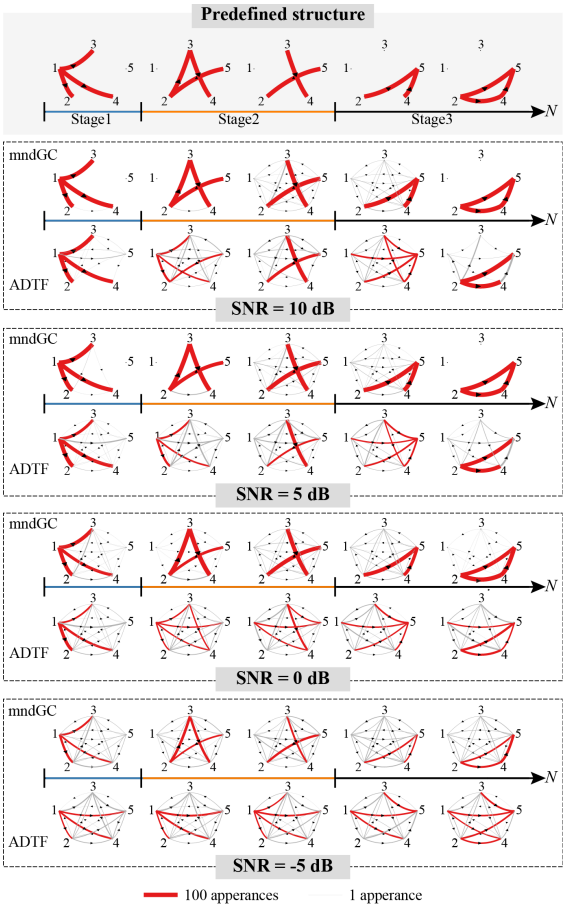

Fig. 2. The time-varying directed network estimated by mndGC and ADTF under various SNR conditions. On the top, is the predefined structure that shows the time-varying patterns that should be recovered over the 100 runs. Below it, each row represents the network varied across the three stages over the 100 runs. In each subfigure, a line with a black arrow on it represents the information flow between two nodes and the thickness of it denotes the total numbers it appears. The line marked in red indicates this line appears more than $\mu + \sigma$ times, with μ and σ representing the mean value and standard deviation of all the connections' appearance times in the estimated network, respectively.

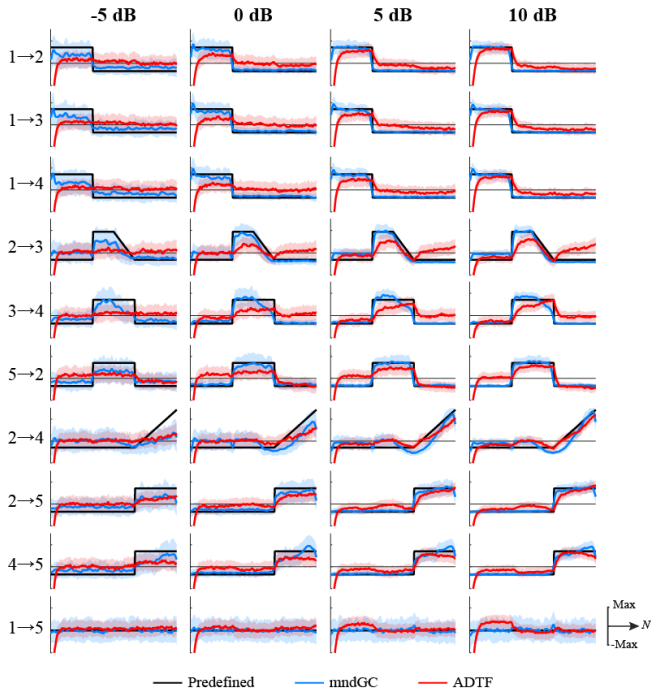

Fig. 3. The normalized connection strength variation of the 100 runs under various SNRs. Each subfigure represents the causality variation between two nodes. The black line is the predefined MVAAR coefficients. The blue and red lines denote the mean time-varying causality strength of the 100 runs of mndGC and ADTF, respectively. The shades with the same color next to them are the corresponding standard deviations. The predefinition of connection $1 \rightarrow 5$ is not normalized since it is a zero vector.

Then, we conducted 100 simulation experiments. In each experiment, 15 trials of multivariate signals were generated according to equation (14). Each trial consisted of 5 time series which last 3 seconds with a sampling frequency of 100 Hz. Subsequently, the Gaussian noises with different signal-to-noise ratios (SNRs), i.e., SNR $= -5$, 0, 5, 10, were added to each trial. Finally, using mndGC and ADTF, we estimated the time-varying connectivity matrices (dimension: $5 \times 5 \times 300$) for the 100 experiments. Consistent with the predefinitions, the top-ranked 3 connections at each time point formed the final binarized network.

2) Simulation Assessments: Fig. 2. shows the reconstructed time-varying directed network by mndGC and ADTF. Each row represents the network varied across the three stages with representative patterns. The thickness of a line indicates the number that this connection was recovered out of 100 runs. The red lines indicate the connections with higher appearance times. The more the network composed of these connections is consistent with the predefined structure, the better performance the corresponding method has.

Comparatively, under different SNR conditions, the network estimated by mndGC has a more consistent structure with the predefined one, i.e., the thicker red lines are mostly overlapped with the true patterns. While ADTF has disturbed network structures, even at the highest SNR (10 dB), the red lines still have structures that are different from the predefinitions. Under the low SNRs like -5 dB and 0 dB, though the performance is lowered, mndGC still can recover the fundamental predefined networks with large overlaps between the red linkages and predefined linkages. However, the network pattern recovered by ADTF is almost corrupted, where there is very little consistency between the red linkages and the ground truth.

The variation of connection strength gives further evidence to reflect the performance between the two approaches. Here 9 connections that have different values across the three stages (information flow changes over time) and 1 connection $1 \rightarrow 5$ as a representative connection that always keeps 0 (no causality relationship) during the whole process were shown in Fig. 3. For better visualization, except for predefinitions of connection $1 \rightarrow 5$ that is a zero vector, all the other strength time courses of these connections were normalized to a uniform scale using z-scores.

As shown in Fig. 3, compared to ADTF, under each noise condition, the connection strength curves estimated by mndGC are more consistent (almost overlapped under 5 dB and 10 dB)

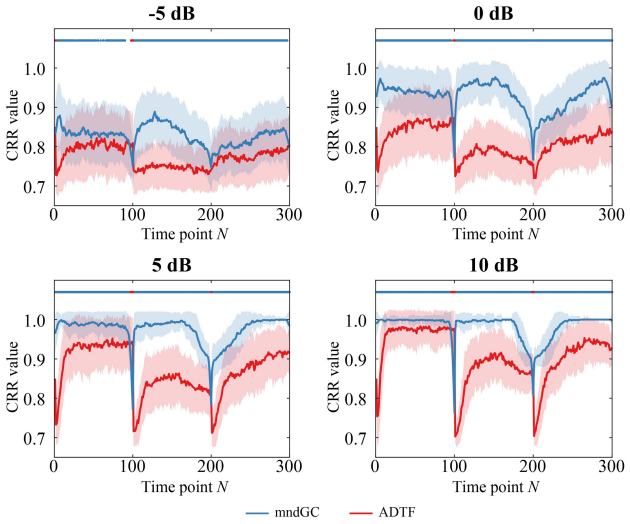

Fig. 4. The tv-CRRs obtained by mndGC and ADTF under the various SNR conditions. The blue and red solid lines denote the mean tv-CRRs of the 100 runs calculated by mndGC and ADTF, respectively. The shades with the same color next to them are the corresponding standard deviations. The blue dot indicates the CRR value of mndGC is significantly higher than that of ADTF, and in contrast, the red dot represents the CRR value of ADTF is significantly higher ($p < 0.05$).

TABLE I
THE m-CRR WITH INCREASING SNR

Method	-5 dB	0 dB	5 dB	10 dB
mndGC	**0.83±0.01***	**0.93±0.01***	**0.97±0.01***	**0.98±0.00***
ADTF	0.77±0.01	0.81±0.01	0.87±0.01	0.91±0.01

The value in a bold type with a red star denotes the m-CRR of mndGC is significantly higher than ADTF ($p<0.000$).

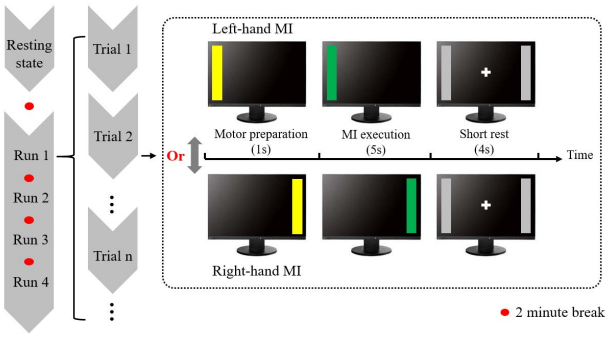

Fig. 5. The MI paradigm used in this study.

with the predefined MVAAR coefficients series, where the fundamental fluctuation trends could be well recovered under all SNRs. While ADTF only can capture the time-varying MVAAR patterns under the relatively higher SNRs like 5 and 10 dB. When a signal is contaminated with stronger noise like 0 and −5 dB, ADTF fails to track the fluctuation patterns well. In addition, when edge linkage strength changes to a new state, ADTF will need a relatively long transition duration to adapt to this change, while mndGC can capture this change timely.

To quantitatively assess the performance of mndGC, we further defined the ratio of the correctly recovered connections to the total connections (20 in this study) in a network at a specific time point as,

$$\mathrm{CRR}(t) = \frac{G_C(t)}{G_T(t)} \tag{18}$$

where $G_C(t)$ and $G_T(t)$ are the number of correctly recovered edges and the total edges (20 for a 5-node network) in the network at that time point, respectively. The $\mathrm{CRR}(t)$ was calculated at each time point in each experiment and the time-varying CRR (tv-CRR) and mean CRR (m-CRR) across all the time points are presented in Fig. 4 and TABLE I, respectively. As demonstrated in Fig. 4, under each noise condition, the mndGC has statistically higher tv-CRR ($p < 0.05$) and m-CRR ($p < 0.000$) values compared to ADTF at almost all time points.

B. Real Data Application: MI EEG Data Set

1) Data Recording and Preprocessing: The experiment was authorized by the Institution Ethics Committee of the University of Electronic Science and Technology of China. Twenty-seven healthy right-handed graduate students with normal or correct-to-normal vision (females 9, ages ranged from 19 to 26 years) were recruited to participate in our experiment. They neither are alcohol or drug addicts nor have cognitive dysfunctions or neurological impairments. Before the experiment, the experimenter would explain the MI task guidelines to participants in detail and collect their signed written informed consent.

The environment preparations and procedures of our experiment follow the standard MI paradigm, and the procedures are given in Fig. 5. In the beginning, 2-minute eyes-closed resting-state EEG data were collected, then, 4-run of MI tasks follows, in which a 2-minute break was allowed between two runs. Each run contains 50 trials, 25 left-hand and 25 right-hand MI trials, the left- and right-hand trials appear on the screen randomly. Each trial consisted of a 1-second cue (yellow bar lay on the left or right side of the screen), 5-second MI execution (green bar lay on the same position), and 4-second short break (gray bar lay on both sides of the screen). The left and right positions of the yellow and green bar indicated the left and right MI tasks, respectively. Once the bar turned green, the participant was required to accomplish the imagery of bouncing a ball in 5 seconds. Any real hand movement would lead to a stop of the experiment.

Using the Symtop amplifier (Symtop Instrument, Beijing, China), EEG signals were recorded by 15 Ag/AgCl electrodes (i.e., F3, F4, FC3, FC4, Cz, C3, C4, C5, C6, CP3, CP4, P3, P4, O1, and O2) that follow the 10-20 system and digitized with a sampling rate of 1000 Hz. There are also three additional electrodes, in which vertical and horizontal EOG were used to detect the eyes' activities and AFz serves as the reference. All electrode impedance was set below 10 kΩ and the online band-pass filter is 0.5-45Hz.

To obtain the clean MI related data, the raw EEG signals were preprocessed by the following procedures, including Reference electrode standardization technique (REST)

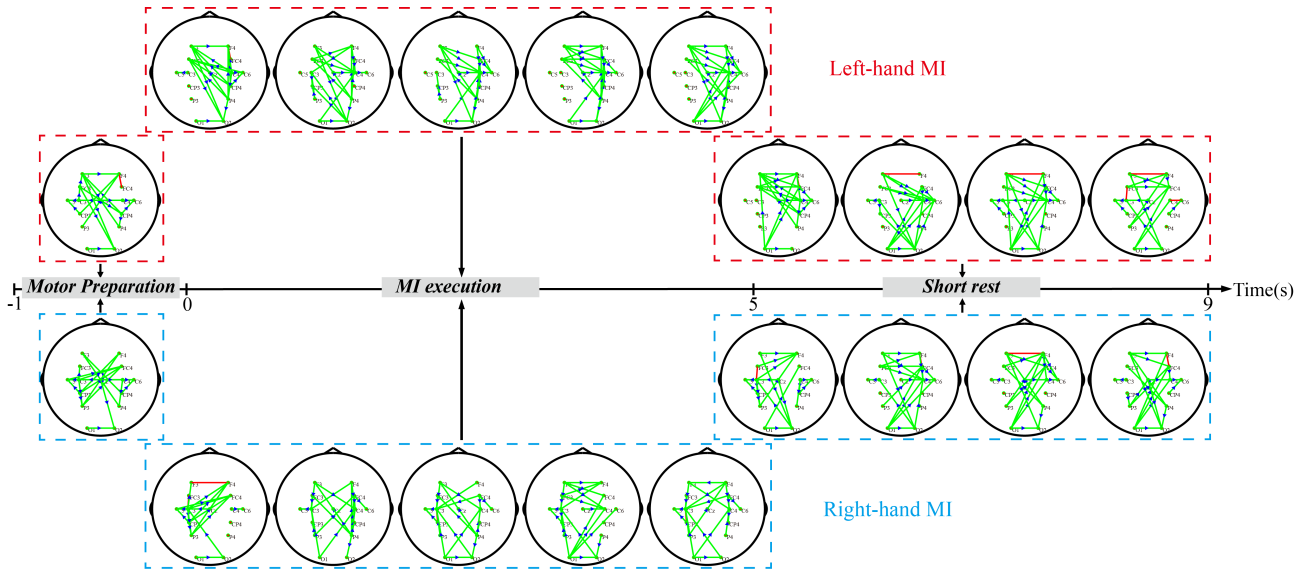

Fig. 6. MI time-varying directed network for the left- and right-hand MIs. The long black arrow indicates the time; above it, the subfigures surrounded by the red dash lines denote the time-varying directed networks for left-hand MI; below it, the subfigures surrounded by the blue dash lines represent the time-varying directed networks for right-hand MI. In each subfigure, a green line with an arrow indicates the information flow between electrodes (brain areas), and the red line denotes bidirectional connection.

referencing [47], 8-30 Hz bandpass filtering, [−1s, 9s] data segmenting (0 s denotes when the green bar appears, i.e., the time that participants starting to executing MI action), and artifact trials removal with a threshold of ± 70 μv. Then, the obtained clean MI-related EEG trials were down-sampled to 100 Hz for subsequent analysis. With such procedures, each trial consists of a 1-second "Motor preparation", a 5-second MI execution, and a 4-second after-task short resting state.

2) MI Time-Varying Directed EEG Network: As MI mostly involves the μ (8-13) rhythm [48], ith mndGC and ADTF, the MI time-varying directed EEG network was constructed in this band for both left- and right-hand MIs of each subject. The mean time-varying directed connectivity matrix of the 27 subjects is taken as the final connectivity matrix. Then, consistent with the previous study, a cost threshold strategy (keep the top 10% connections in the network) was used to binarize the connectivity matrices [49], [50]. The different time-varying directed networks for different kinds of MI consisting of three stages (1-second "Motor preparation", 5-second "MI execution", and 4-second "Short rest") with a time interval of 1 second were shown in Fig. 6 for mndGC and Fig. S1 for ADTF (see supplementary materials).

Compared to ADTF, the network of mndGC shows more distinct stage characteristics for the left- and right-hand MI. The "Motor preparation" stage shows bilateral and symmetry connections that originate from sensorimotor areas. During the "MI execution" stage, the network has distinguishable patterns (i.e., contralateral lateralization, the left-hand MI has more right-hemisphere directed connections and right-hand MI has more left-hemisphere directed connections) between left- and right-hand MIs and the lateralization of left-hand MI is comparatively more prominent. Then, such lateralization gradually fades out during the "Short rest" stage. Finally, in the late "Short rest" period, the network reverts the bilateral and symmetric activities characterized by comparatively decreasing motor areas and increasing frontal and occipital connections for both two MI tasks. Besides, the time-varying directed networks under different thresholds (i.e., 5%, 15%, and 20%) show similar patterns as that under the 10% threshold, which consistently demonstrates the reliability of the identified network patterns by our developed mndGC. While for the ADTF, during the whole process, the network shows stable motor area activities and a degree of contralateral lateralization, the stage character is a little blurred.

The out-degree is a kind of network measurement that assesses the centrality (specifically, the origin and the propagation characteristics) of a node [51]. To investigate such characters quantitatively during the MI process, we further calculated the time-varying out-degree in the left- and right-side brain, respectively, for each subject based on the network. Following the brain connectivity toolbox (BCT, http://www.nitrc.org/projects/bct/) [51], the out-degree of the left-hemisphere brain is computed at each time point as,

$$D(t) = \sum\nolimits_{m \in \Lambda_{left}} \sum\nolimits_{n \in \Lambda} d(t)_{mn}, \quad m \neq n \tag{19}$$

where $d(t)_{mn}$ denotes the outflow from node m to n (if yes $d(t)_{mn} = 1$, else $d(t)_{mn} = 0$), Λ indicates the set of all nodes in the network, and Λ_{left} is the left-hemisphere brain electrodes set. The left- and right-hemisphere electrodes sets were divided according to the 10-20 system. Specifically, after excluding the midline electrodes, the odd/even status of the number in the electrode name determines whether this electrode belongs to the left or right hemisphere (i.e., odd-left, even-right) [52]. The variations of the left-and right-hemisphere brain hemisphere out-degree across the 27 subjects were shown in Fig. 7 for mndGC and Fig. S2 for ADTF (see supplementary materials). For mndGC, the hemisphere outdegree shows evident stage characters. For left-hand MI,

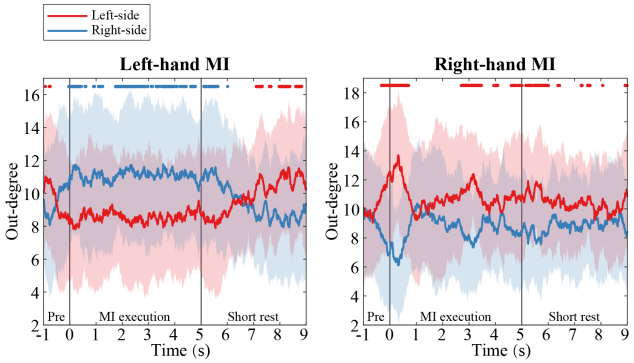

Fig. 7. Time-varying directed network out-degree evolution of left- and right-hand MIs. The abbreviation "Pre" denotes stage "Motor preparation". The red and blue lines indicate the mean time-varying out-degree across the 27 subjects, respectively, and the corresponding shade denotes the standard deviation. The blue dot represents the out-degree of right-hemisphere brain regions is significantly higher than the left hemisphere, and the red dot means the out-degree of left-hemisphere brain regions is significantly higher than that of the right hemisphere ($p < 0.05$).

during the early "Motor preparation" and the late "Short rest" period, the out-degree of left-hemisphere regions is significantly higher than the right-hemisphere regions, while during the "MI execution" period, the out-degree of right-hemisphere regions is significantly higher. For right-hand MI, most of the time, the left-hemisphere brain has a significantly higher out-degree than the right hemisphere, especially around the early and late "MI execution" period. As it moves away from the "MI execution" period (i.e., the early "Motor preparation" and late "Short rest"), the left- and right-hemisphere brain out-degrees gradually become no significant difference. Whereas for ADTF, the network maintains higher contralateral hemisphere outdegree during the three stages and shows significance during the "MI execution" and late "Short rest" periods.

IV. Discussion

EEG-based time-varying directed network analysis is of great importance in investigating the dynamical causality among multiple brain areas and discovering the key intervention targets. In this study, we extend the nonparametric time-varying directed EEG network explorations with mndGC to avoid the parametric trap of the traditional methods represented by the most widely use ADTF.

The simulation study evaluated the performance of mndGC compared to the traditional parametric ADTF under different noise conditions, through network patterns, connection strength variations, tv-CRR, and m-CRR values. As shown in Fig. 2, the time-varying directed network estimated by mndGC has better consistency (i.e., consistent structure indicated by red lines and fewer pseudo connections) than ADTF under each noise condition. The significantly higher tv-CRR (Fig. 4) and m-CRR (TABLE I) of mndGC than those of ADTF also give intuitive numerical evidence. In essence, the time-varying network patterns are determined by how the time-varying MVAAR coefficients could be tracked. As shown in Fig. 3, the connection strength recovered by mndGC is more consistent with the predefined MVAAR coefficients, and their fluctuation trends are almost overlapped under the high SNR condition, e.g., 10 dB and 5 dB (Fig. 3). However, as for ADTF, the true fluctuation of MVAAR coefficients cannot be well tracked, especially under the relatively lower 0 and −5 dB SNRs, most of the state change information is missed. This difference accounts for the performance difference between the two approaches. The better performance of mndGC attributes much to the direct calculation of the causality in a data-driven way. The performance of the parametric approach relies a lot on the accurate modeling of the data. Although Kalman filter is comparatively good at getting the adapt MVAR parameters compared to the sliding window strategies [22], [53], as Kalman filter applied the continuous assumption for state changes, ADTF takes a relatively long duration to reach stability [22], [54], which will fail to capture the states with abrupt changes when the network state changes to another new one as shown in Fig.3. Consequently, mndGC is more noise-resistant and more competitive at capturing the instantaneous directed network changes flexibly.

As a multidimensional and dynamical high-level cognition process, MI has gained much attention in recent years. Knowledge of time-varying directed networks helps a lot in revealing the underlying mechanism of efficient MI processing, which will further profit the more efficient MI BCI and motor rehabilitation system. In this study, considering the good performance of mndGC, we applied it to the real EEG MI data set and observed the dynamical information flow in the brain during the MI process in the μ band, whose oscillations are demonstrated to be important for MI processing [48], [55], [56].

During the "Motor preparation" stage, considering the subject is waiting for a MI stimulus, the time-varying directed network show relatively symmetric sensorimotor areas activities are reasonable. As is reported, brain contralateral lateralization is an essential characteristic of the MI process [18], [43], [57], therefore, during the period of MI processing and execution, the networks of different MIs during the "MI execution" stage show distinct lateralization (i.e., the left-hand MI show more right-hemisphere directed connections, while right-hand MI show more left-hemisphere directed connections). Then, the lateralization gradually fades out and reverts the bilateral and symmetric activities with decreasing motor areas and increasing frontal and occipital areas activities during the "Short rest" stage. After finishing the MI task, the brain is essentially at a resting state, and therefore shows the default-mode-network-like long-range connections between frontal and occipital areas. These stage characteristics can only be revealed clearly by mndGC (Fig. 6). As for ADTF, the networks show lateralization sustainability, while the stage characteristics of the three stages are a little blurred, except during the "Motor preparation" stage, the network patterns in the rest of the process are relatively similar.

The network hemisphere out-degree further gives the quantitative indicator, i.e., the causality dominance of left- and right-brain of such laterality during MI processes [51]. As shown in Fig.7, mndGC can trace the network changes well. Consistent with the network topology and previous

studies [18], [58], the brain contralateral hemisphere out-degree is significantly higher during the "MI execution" period both for left- and right-hand MIs. During the early "Motor preparation" and late "Short rest" stage, left-hand MI has a significantly higher left hemisphere out-degree, while for right-hand MI, although not significant, its left hemisphere out-degree is also relatively higher. This is probably due to that all the subjects recruited for our study are right-handed. The long history of using the right hand has already enhanced the relevant functions in the left-side brain [18]. This is also why the network lateralization of the easier right-hand task is less obvious, e.g., the network during "MI execution" of mndGC (Fig. 6, and Fig. S1) and the network of ADTF (Fig. 7 and Fig. S2). As for ADTF (Fig. S2), the relatively higher contralateral hemisphere out-degree keeps during the whole three stages, it cannot trace the brain state changes immediately. That is coincident with the fact that the ADTF needs a relatively long duration to reach stability. It is fair to say that constructing the time-varying directed EEG network with a nonparametric approach, i.e., mndGC in this study, has a nice performance in mining the instantaneous directed network changes.

V. Conclusion

In this study, we proposed to construct a time-varying directed EEG network in a nonparametric data-driven way with mndGC instead of the traditional parametric approaches represented by the most widely used ADTF. simulation study demonstrated that the mndGC is more noise-resistant and better at capturing the instantaneous directed network changes compared to ADTF. As applications in real MI EEG data, the mndGC also reveals more distinct network stage characters. Therefore, mndGC is worthy of consideration for the time-varying directed EEG network analysis, as well as the extensive neurophysiological signals. Our study extends the exploration of mining the causality operation mechanisms in the brain with time-varying directed EEG networks in a nonparametric and data-driven way and provides practical experience and suggestions.

References

[1] H.-J. Park and K. Friston, "Structural and functional brain networks: From connections to cognition," *Science*, vol. 342, no. 6158, Nov. 2013.

[2] O. Sporns, "Making sense of brain network data," *Nature Methods*, vol. 10, p. 491, Jun. 2013.

[3] T. Ito, L. Hearne, R. Mill, C. Cocuzza, and M. W. Cole, "Discovering the computational relevance of brain network organization," *Trends Cognit. Sci.*, vol. 24, no. 1, pp. 25–38, Jan. 2020.

[4] V. Menon, "Developmental pathways to functional brain networks: Emerging principles," *Trends Cognit. Sci.*, vol. 17, no. 12, pp. 627–640, Dec. 2013.

[5] F. Li *et al.*, "The construction of large-scale cortical networks for P300 from scalp EEG," *IEEE Access*, vol. 6, pp. 68498–68506, 2018.

[6] C. Yi *et al.*, "A novel method for constructing EEG large-scale cortical dynamical functional network connectivity (dFNC): WTCS," *IEEE Trans. Cybern.*, early access, Aug. 16, 2021, doi: 10.1109/TCYB.2021.3090770.

[7] J. C. Bore *et al.*, "A long short-term memory network for sparse spatiotemporal EEG source imaging," *IEEE Trans. Med. Imag.*, vol. 40, no. 12, pp. 3787–3800, Dec. 2021.

[8] R. Zhang *et al.*, "Efficient resting-state EEG network facilitates motor imagery performance," *J. Neural Eng.*, vol. 12, no. 6, Dec. 2015, Art. no. 066024.

[9] F. Li *et al.*, "Differentiation of schizophrenia by combining the spatial EEG brain network patterns of rest and task P300," *IEEE Trans. Neural Syst. Rehabil. Eng.*, vol. 27, no. 4, pp. 594–602, Apr. 2019.

[10] P. Li *et al.*, "EEG based emotion recognition by combining functional connectivity network and local activations," *IEEE Trans. Biomed. Eng.*, vol. 66, no. 10, pp. 2869–2881, Oct. 2019.

[11] C. Yi *et al.*, "Constructing large-scale cortical brain networks from scalp EEG with Bayesian nonnegative matrix factorization," *Neural Netw.*, vol. 125, pp. 338–348, May 2020.

[12] F. Li *et al.*, "The time-varying networks in P300: A task-evoked EEG study," *IEEE Trans. Neural Syst. Rehabil. Eng.*, vol. 24, no. 7, pp. 725–733, Jul. 2016.

[13] J. Cao *et al.*, "Brain functional and effective connectivity based on electroencephalography recordings: A review," *Hum. Brain Mapping*, vol. 43, no. 2, pp. 860–879, Feb. 2022.

[14] M. Hassan and F. Wendling, "Electroencephalography source connectivity: Aiming for high resolution of brain networks in time and space," *IEEE Signal Process. Mag.*, vol. 35, no. 3, pp. 81–96, May 2017.

[15] F. Li *et al.*, "Brain variability in dynamic resting-state networks identified by fuzzy entropy: A scalp EEG study," *J. Neural Eng.*, vol. 18, no. 4, Aug. 2021, Art. no. 046097.

[16] J. C. Bore *et al.*, "Sparse EEG source localization using LAPPS: Least absolute l-P (0<p<1) penalized solution," *IEEE Trans. Biomed. Eng.*, vol. 66, no. 7, pp. 1927–1939, Jul. 2019.

[17] Y. Si *et al.*, "Different decision-making responses occupy different brain networks for information processing: A study based on EEG and TMS," *Cerebral Cortex*, vol. 29, no. 10, pp. 4119–4129, Sep. 2019.

[18] F. Li *et al.*, "The dynamic brain networks of motor imagery: Time-varying causality analysis of scalp EEG," *Int. J. Neural Syst.*, vol. 29, no. 1, Feb. 2019, Art. no. 1850016.

[19] P. Song *et al.*, "Repetitive transcranial magnetic stimulation (rTMS) modulates time-varying electroencephalography (EEG) network in primary insomnia patients: A TMS-EEG study," *Sleep Med.*, vol. 56, pp. 157–163, Apr. 2019.

[20] B. He *et al.*, "Electrophysiological brain connectivity: Theory and implementation," *IEEE Trans. Biomed. Eng.*, vol. 66, no. 7, pp. 2115–2137, Jul. 2019.

[21] M. F. Pagnotta and G. Plomp, "Time-varying MVAR algorithms for directed connectivity analysis: Critical comparison in simulations and benchmark EEG data," *PLoS ONE*, vol. 13, no. 6, Jun. 2018, Art. no. e0198846.

[22] C. Wilke, L. Ding, and B. He, "Estimation of time-varying connectivity patterns through the use of an adaptive directed transfer function," *IEEE Trans. Biomed. Eng.*, vol. 55, no. 11, pp. 2557–2564, Nov. 2008.

[23] L. Astolfi *et al.*, "Comparison of different cortical connectivity estimators for high-resolution EEG recordings," *Hum. Brain Mapping*, vol. 28, pp. 143–157, Feb. 2007.

[24] P. P. Mitra and B. Pesaran, "Analysis of dynamic brain imaging data," *Biophys. J.*, vol. 76, no. 2, pp. 691–708, Feb. 1999.

[25] R. F. Helfrich *et al.*, "Neural mechanisms of sustained attention are rhythmic," *Neuron*, vol. 99, no. 4, pp. 854–865, 2018.

[26] X. Shan *et al.*, "A revised Hilbert–Huang transformation to track non-stationary association of electroencephalography signals," *IEEE Trans. Neural Syst. Rehabil. Eng.*, vol. 29, pp. 841–851, 2021.

[27] F. Li *et al.*, "Reconfiguration of brain network between resting state and P300 task," *IEEE Trans. Cognit. Develop. Syst.*, vol. 13, no. 2, pp. 383–390, Jun. 2021.

[28] L. Harrison, W. D. Penny, and K. Friston, "Multivariate autoregressive modeling of fMRI time series," *NeuroImage*, vol. 19, no. 4, pp. 1477–1491, Aug. 2003.

[29] D. G. Brooks, "Akaike information criterion statistics," *Technometrics*, vol. 31, no. 2, pp. 270–271, May 1989.

[30] G. Schwarz, "Estimating the dimension of a model," *Ann. Statist.*, vol. 6, no. 2, pp. 461–464, Mar. 1978.

[31] M. Dhamala, G. Rangarajan, and M. Ding, "Estimating Granger causality from Fourier and wavelet transforms of time series data," *Phys. Rev. Lett.*, vol. 100, no. 1, Jan. 2008, Art. no. 018701.

[32] J. Geweke, "Measurement of linear dependence and feedback between multiple time series," *J. Amer. Stat. Assoc.*, vol. 77, no. 378, pp. 304–313, Jun. 1982.

[33] X. Wen, G. Rangarajan, and M. Ding, "Multivariate Granger causality: An estimation framework based on factorization of the spectral density matrix," *Phil. Trans. Roy. Soc. A, Math., Phys. Eng. Sci.*, vol. 371, no. 1997, Aug. 2013, Art. no. 20110610.

[34] M. F. Pagnotta, M. Dhamala, and G. Plomp, "Benchmarking non-parametric Granger causality: Robustness against downsampling and influence of spectral decomposition parameters," *NeuroImage*, vol. 183, pp. 478–494, Dec. 2018.
[35] M. Dhamala *et al.*, "Analyzing information flow in brain networks with nonparametric Granger causality," *NeuroImage*, vol. 41, pp. 354–362, Jun. 2008.
[36] I. Winkler, D. Panknin, D. Bartz, K.-R. Müller, and S. Haufe, "Validity of time reversal for testing Granger causality," *IEEE Trans. Signal Process.*, vol. 64, no. 11, pp. 2746–2760, Jun. 2016.
[37] S. Honjoh, S. Sasai, S. S. Schiereck, H. Nagai, G. Tononi, and C. Cirelli, "Regulation of cortical activity and arousal by the matrix cells of the ventromedial thalamic nucleus," *Nature Commun.*, vol. 9, no. 1, p. 2100, Dec. 2018.
[38] F. D. Weber, G. G. Supp, J. G. Klinzing, M. Mölle, A. K. Engel, and J. Born, "Coupling of gamma band activity to sleep spindle oscillations—A combined EEG/MEG study," *NeuroImage*, vol. 224, Jan. 2021, Art. no. 117452.
[39] F. Li *et al.*, "Inter-subject P300 variability relates to the efficiency of brain networks reconfigured from resting- to task-state: Evidence from a simultaneous event-related EEG-fMRI study," *NeuroImage*, vol. 205, Jan. 2020, Art. no. 116285.
[40] M. Lotze and U. Halsband, "Motor imagery," *J. Physiol. Pairs*, vol. 99, pp. 386–395, Feb. 2006.
[41] R. Abiri, S. Borhani, E. W. Sellers, Y. Jiang, and X. Zhao, "A comprehensive review of EEG-based brain–computer interface paradigms," *J. Neural Eng.*, vol. 16, no. 1, Feb. 2019, Art. no. 011001.
[42] G. Pfurtscheller and C. Neuper, "Motor imagery activates primary sensorimotor area in humans," *Neurosci. Lett.*, vol. 239, pp. 65–68, Dec. 1997.
[43] S. Hu, H. Wang, J. Zhang, W. Kong, Y. Cao, and R. Kozma, "Comparison analysis: Granger causality and new causality and their applications to motor imagery," *IEEE Trans. neural Netw. Learn. Syst.*, vol. 27, no. 7, pp. 1429–1444, Jul. 2016.
[44] C. Torrence and G. P. Compo, "A practical guide to wavelet analysis," *Bull. Amer. Meteorolog. Soc.*, vol. 79, no. 1, pp. 61–78, 1998.
[45] G. T. Wilson, "The factorization of matricial spectral densities," *SIAM J. Appl. Math.*, vol. 23, no. 4, pp. 420–426, Dec. 1972.
[46] R. Oostenveld, P. Fries, E. Maris, and J.-M. Schoffelen, "FieldTrip: Open source software for advanced analysis of MEG, EEG, and invasive electrophysiological data," *Comput. Intell. Neurosci.*, vol. 2011, pp. 1–9, Oct. 2011.
[47] L. Dong *et al.*, "MATLAB toolboxes for reference electrode standardization technique (REST) of scalp EEG," *Frontiers Neurosci.*, vol. 11, p. 601, Oct. 2017.
[48] D. Denis, R. Rowe, A. M. Williams, and E. Milne, "The role of cortical sensorimotor oscillations in action anticipation," *NeuroImage*, vol. 146, pp. 1102–1114, Feb. 2017.
[49] E. Bullmore and O. Sporns, "The economy of brain network organization," *Nature Rev., Neurosci.*, vol. 13, pp. 336–349, May 2012.
[50] C. Yi *et al.*, "Constructing EEG large-scale cortical functional network connectivity based on brain atlas by s estimator," *IEEE Trans. Cognit. Develop. Syst.*, vol. 13, no. 4, pp. 769–778, Dec. 2021.
[51] M. Rubinov and O. Sporns, "Complex network measures of brain connectivity: Uses and interpretations," *NeuroImage*, vol. 52, no. 3, pp. 1059–1069, Sep. 2010.
[52] V. Jurcak, D. Tsuzuki, and I. Dan, "10/20, 10/10, and 10/5 systems revisited: Their validity as relative head-surface-based positioning systems," *Neuroimage*, vol. 34, no. 4, pp. 1600–1611, 2007.
[53] L. Astolfi *et al.*, "Tracking the time-varying cortical connectivity patterns by adaptive multivariate estimators," *IEEE Trans. Biomed. Eng.*, vol. 55, no. 3, pp. 902–913, Mar. 2008.
[54] T. Schack, M. Muma, M. Feng, C. Guan, and A. M. Zoubir, "Robust nonlinear causality analysis of nonstationary multivariate physiological time series," *IEEE Trans. Biomed. Eng.*, vol. 65, no. 6, pp. 1213–1225, Jun. 2018.
[55] F. Li *et al.*, "Brain network reconfiguration during motor imagery revealed by a large-scale network analysis of scalp EEG," *Brain Topography*, vol. 32, no. 2, pp. 304–314, Mar. 2019.
[56] C. Babiloni *et al.*, "Human movement-related potentials vs desynchronization of EEG alpha rhythm: A high-resolution EEG study," *NeuroImage*, vol. 10, no. 6, pp. 658–665, Dec. 1999.
[57] Q. Gao, X. Duan, and H. Chen, "Evaluation of effective connectivity of motor areas during motor imagery and execution using conditional Granger causality," *NeuroImage*, vol. 54, no. 2, pp. 1280–1288, Jan. 2011.
[58] G. Pfurtscheller, C. Brunner, A. Schlögl, and F. H. L. da Silva, "Mu rhythm (de)synchronization and EEG single-trial classification of different motor imagery tasks," *NeuroImage*, vol. 31, no. 1, pp. 153–159, 2006.